Materials Today Physics 13 (2020) 100216

Contents lists available at ScienceDirect

Materials Today Physics

journal homepage: https://www.journals.elsevier.com/materials-today-physics

Outstanding oxygen evolution reaction performance of nickel iron selenide/stainless steel mat for water electrolysis

S. Song [a], L. Yu [a], X. Xiao [a], Z. Qin [b], W. Zhang [a], D. Wang [a], J. Bao [b], H. Zhou [c, f], Q. Zhang [d], S. Chen [a, **], Z. Ren [a, *]

[a] Department of Physics, Texas Center for Superconductivity at the University of Houston (TcSUH), University of Houston, Houston, TX 77204, USA
[b] Department of Electrical and Computer Engineering, University of Houston, Houston, TX 77204, USA
[c] Synergetic Innovation Center for Quantum Effects and Applications, Key Laboratory of Low-Dimensional Quantum Structures and Quantum Control of Ministry of Education, School of Physics and Electronics, Hunan Normal University, Hunan 410081, China
[d] Key Laboratory of Fluid and Power Machinery of Ministry of Education, School of Materials Science and Engineering, Xihua University, Chengdu 610039, China
[f] Key Laboratory for Matter Microstructure and Function of Hunan Province, Hunan Normal University, Changsha 410081, China

ARTICLE INFO

Article history:
Received 5 February 2020
Received in revised form
26 March 2020
Accepted 26 March 2020
Available online 8 April 2020

Keywords:
Oxygen evolution reaction
Nickel iron selenide
Stainless steel mat
Selenization
Water electrolysis

ABSTRACT

Stainless steel (SS) has been widely incorporated into electrodes or used as a conductive scaffold in industrial water electrolysis. Operations using such SS-bearing materials proceed under substantial overpotentials above the thermodynamic requirement due to the sluggish kinetics of the anodic oxygen evolution reaction (OER). Traditional surface engineering of SS involves a corrosion process to optimize its composition and modify its surface morphology, but its catalytic properties remain unsatisfactory even after employing this technique. Here, we introduce an effective route, based on surface decoration, to construct a ternary phase composed of nickel iron selenide (NiFeSe) uniformly distributed on a stainless-steel mat (SSM). NiFeSe/SSM was found to require an overpotential of only 260 mV to drive a current density of 1,000 mA cm^{-2} at 75°C in alkaline solution, one of the best results among SS-based and even transition metal-based catalysts for OER. Additionally, this NiFeSe/SSM electrode shows negligible potential degradation after operating at 1,000 mA cm^{-2} for 55 h. It is suggested that Se in the nickel iron selenide directly binds to the SSM through strong covalent bonding during selenization, which guarantees low charge-transfer resistance and excellent durability against the gas bubbles produced during operation at large current densities. This work opens a new route for performing surface engineering on SS or other conductive substrates to achieve superior OER performance.

Introduction

Growing fossil fuel consumption and its associated environmental issues have led to great concern [1,2]. Seeking renewable and eco-friendly energy alternatives to target these issues is essential in the next few decades [3,4]. Hydrogen generated by electrochemical water splitting is one of the most promising candidates. Intermittent solar-, wind-, or thermal-derived electricity and redundant electric power can be chemically stored as hydrogen generated by electrochemical water splitting, whereas pure water is the only product when hydrogen is converted back to obtain electricity *via* combustion or fuel cells [5–8].

Electrochemical water splitting consists of two half-reactions, hydrogen evolution reaction (HER) and oxygen evolution reaction (OER) [9,10]. Thermodynamically, initiating the full cell reaction requires overcoming the potential barrier of 1.23 V, but kinetically, a considerable amount of extra potential is necessary [11,12]. OER is the major obstacle for the large-scale application of water splitting due to the multiple steps of proton-coupled electron transfer and the high formation energy of oxygen-oxygen bonding [13]. State-of-the-art OER catalysts are based on noble metal oxides IrO_2 and RuO_2, but their scarcity and high cost pose great constraints to practical use [14,15]. In contrast, non-noble metal-based catalysts contain low-cost and earth-abundant elements, and some of them exhibit catalytic kinetics that outperform the noble-metal catalysts

* Corresponding author.
** Corresponding author.
E-mail addresses: schen34@uh.edu (S. Chen), zren@uh.edu (Z. Ren).

https://doi.org/10.1016/j.mtphys.2020.100216
2542-5293/

in alkaline electrolyte [16–18]. Transition-metal chalcogenides have been widely investigated as efficient catalysts for HER and OER [19,20]. Our previous work has demonstrated that excellent OER catalysts, NiFe selenides, are easily converted to NiFe hydroxides by a simple cyclic voltammetry (CV) activation process in alkaline electrolyte [21].

In addition to the catalysts, their substrates also play important roles in cell performance. Traditionally, stainless steel (SS)-based substrates have been used industrially for electrochemical water splitting in alkaline media due to their low cost and high corrosion resistance [22–25], but they suffer from relatively high OER overpotentials, normally requiring an overpotential of ~350–370 mV to achieve a current density of 10 mA cm^{-2} in 1 M KOH [26,27]. One reason for this is the high Cr content in SS, which is normally detrimental to, or inert in, the catalytic performance [27–30]. Another challenge is that the SS composition of over 70% Fe falls outside the optimal Ni/Fe ratio range [21,31,32]. To reduce the overpotential for OER, different methods for SS surface modification and decoration have been demonstrated, such as corrosion engineering [27,33,34], electrochemical CV scanning [22,35], electrodeposition [29], sol-gel chemistry [23], *etc.* The most common method has been to generate NiFe hydroxides by self-corrosion under a large oxidation current at an elevated temperature. NiFe hydroxides have been widely found to exhibit high kinetics for OER in base and to facilitate the electron transfer at the interface [36]. A thin Ni/Fe oxide layer on the surface of AISI 304 was acquired by Schafer *et al.* after exposing the surface to oxidation under a current density of around 1,800 mA cm^{-2} in 7.2 M NaOH at 50°C for hundreds of minutes, promoting its OER performance to achieve a current density of 12 mA cm^{-2} at an overpotential of 212 mV in 1 M KOH [35]. Anantharaj *et al.* used a controlled corrosion-engineering process on AISI 304 by hydrothermally treating it with a mixed equimolar solution (0.01 M) of KOH and NaOCl at 180°C, which resulted in NiO-incorporated Fe_2O_3 nanocrystals on the surface [28]. The obtained anodes can drive a current density of 10 mA cm^{-2} at an overpotential of 260 mV. Different coatings have also been introduced on SS. For example, a Ni–Co oxide coating was deposited on AISI 304 *via* simple potentiostatic electrodeposition and subsequent annealing, resulting in an overpotential of 530 mV needed to achieve a current density of 10 mA cm^{-2} in 0.1 M KOH [33]. All of these methods suggested that increasing the catalytic activity of SS involves the transformation of the SS surface into Ni/Fe oxides or hydrous oxides on the surface, which had already been extensively demonstrated to be the active sites for OER [37,38]. Recent improvement on SS-based anodic catalysts was reported by Liu et al., who introduced M-Fe-layered double hydroxides (LDHs) (M = Ni^{2+}, Co^{2+}, Mn^{2+}, or Mg^{2+}) on the surfaces of Cr-free iron plates by corrosion engineering, creating ultra-thin LDHs with abundant grain boundaries through *in situ* electrochemical growth. They found that a NiFe-LDH/Fe plate anode can achieve a current density of 40 mA cm^{-2} at an overpotential of 300 mV in 1 M KOH at room temperature, whereas NiFe-LDH/Fe foam can drive a current density of 500 mA cm^{-2} at the same overpotential due to the increased loading mass and electrochemically active surface area (ECSA) [34]. The performance enhancement is attributed to the higher density of exposed catalytically active sites, lower charge-transfer resistance, and higher kinetic activity. However, these results have not prompted industrial adoption of this reported design and process.

In order to attain competitive performance on SS, the following principles should be followed: (1) Ni/Fe oxides or hydroxides on the SS surface act as the active sites and should be easily accessible, at the same time the Ni/Fe ratio also needs to be taken into account; (2) adhesion between the catalyst and the substrate should be strong enough to survive under intense bubbling and should also exhibit low charge-transfer resistance; (3) a three-dimensional structure has the great advantage of exposing more active sites; and (4) cost is always a major concern for large-scale applications. Ideal catalysts are expected to afford a high current density at a low overpotential and simultaneously to have as little loading mass as possible.

In this work, a facile and cost-effective stainless-steel mat (SSM)–based catalyst for OER is developed. Optimized NiFe selenide powder with an optimized Ni/Fe ratio is acquired by ball milling and then dispersed evenly on a SSM. The powder is firmly joined to the SSM by strong covalent bonding resulting from selenization during high-temperature annealing, which ensures excellent electrical and mechanical contact between the active layer and the SSM. In 1 M KOH, the combined electrode is able to drive a current density of 10 mA cm^{-2} at an overpotential of 230 mV and to achieve a large current density of 1,000 mA cm^{-2} at an overpotential of 330 mV. The overpotential is further lowered to 260 mV needed to achieve a current density of 1,000 mA cm^{-2} at 75°C, making it one of the best freestanding electrodes for OER. When the same process is applied on Ni foam (NF), NiFeSe/NF also exhibits remarkable catalytic performance, achieving a current density of 1,000 mA cm^{-2} at an overpotential of 288 mV. This work provides a simple and innovative method of surface engineering on SS that is found to be effective and productive for OER.

Experimental methods

NiFeSe powder

Nickel powder (99.99%, Alfa Aesar), iron powder (99.99%, Alfa Aesar), vanadium powder (99.99%, Alfa Aesar), and selenium shots (99.9%, Sigma Aldrich) were all used as received. All of the raw materials were weighed according to the required stoichiometric ratio and put into a stainless steel jar (SPEX SamplePrep 8007) in a glovebox with an argon atmosphere (H_2O < 0.1 ppm and O_2 < 0.1 ppm). The fine powder was obtained by high-energy ball milling for 2 h.

Stainless steel and nickel-foam electrodes (NiFeSe/SSM and NiFeSe/NF)

The freshly milled powder was fully mixed into a solution of 150 μL dimethylformamide, 1.35 mL ethanol, and 1 mL deionized water. Each conductive substrate (SSM or NF) was immersed into the solution for 5 s and then removed and air-dried. Each substrate was then placed into a tube furnace and annealed under flowing Ar at 500°C for 6 h.

Selenization of stainless steel mat

Se/SSM was synthesized by direct chemical vapor deposition (CVD) in a tube furnace. The appropriate amount of Se powder was placed upstream of the SSM under flowing Ar. The furnace was quickly raised to 500°C, and this temperature was maintained for 6 h. The sample was subsequently cooled down in the furnace under flowing Ar. To address the safety concerns related to working with Se, the quartz tubes used for the annealing and CVD processes were purposely extended to deposit vaporized Se at the downstream end, and the absorber solution was also added at the end of the gas flow.

Electrochemical characterization

The electrochemical tests were performed *via* a typical three-electrode configuration in 100 mL 1 M KOH electrolyte. Pt and

Hg/HgO were adopted as the counter and reference electrodes, respectively. Therefore, all voltages are against the reference electrode and converted to reversible hydrogen electrode (RHE) scaled by $E_{RHE} = E_{Hg/HgO} + 0.059\ pH + 0.098$.

The polarization curves for OER were recorded by linear sweep voltammetry (LSV) with a scan rate of 2 mV s^{-1} in the range of 1.125–1.625 V vs. RHE. CV scans were conducted over 600 cycles with a scan rate of 50 mV s^{-1} in the range of 1.425 and 1.625 (vs. RHE) before measuring the polarization curves. This process was applied for all samples. Additionally, all of the electrocatalytic measurements were performed at room temperature (22°C), except where otherwise specified. The current interruption method was used to compensate for the iR error.

Materials characterization

Raman spectra were collected using a Horiba JY T64000 Raman spectrometer employing a He–Ne laser with an excitation wavelength of 632.8 nm. The total acquisition time was 60 s. High-resolution X-ray photoelectron spectra were collected using a PHI Quantera XPS scanning microprobe with an Al monochromatic K_α source (15 KV, 20 mA). The chamber pressure was well controlled below 5×10^{-8} Torr. Powder X-ray diffraction spectra analysis was conducted using a PANalytical multipurpose diffractometer with an X'celerator detector (PANalytical X'Pert Pro). The morphology and composition characterizations were conducted using a scanning electron microscope (LEO 1525) and a transmission electron microscope (JEOL 2010F).

Results and discussion

The optimized NiFeSe powder (with atomic ratio Ni/Fe = 3/1) was synthesized by high-energy ball milling, following our previous report [21]. The bare SSM was used as received. The SSM loaded with NiFeSe powder is denoted as NiFeSe/SSM, whereas Se/SSM denotes pure SSM subjected to direct selenization by CVD. Additionally, SSM was processed by the same procedure as for NiFeSe/SSM but with immersion into the solution without NiFeSe powder to serve as a control sample and is denoted as None/SSM. The loading mass on the SSM was reproducibly controlled at around 2~3 mg cm^{-2}. X-ray diffraction (XRD) patterns of SSM and the as-prepared NiFeSe/SSM sample can be found in Fig. 1(a). The as-received SSM displays only one main phase within the detection limit, $Fe_{0.7}Cr_{0.19}Ni_{0.11}$ alloy (PDF#33–0397), corresponding to the normal AISI 304 SS. Three phases other than $Fe_{0.7}Cr_{0.19}Ni_{0.11}$ emerge on the surface of the annealed NiFeSe/SSM, one of which is identified as NiFe diselenides due to the chemical reaction at high annealing temperature. It should be noted that the chemical reaction also merged the NiFeSe and the SSM together. The Se detected on the surface of the SSM most likely comes from the vaporized Se in the NiFeSe powder. Other oxides ($NiCr_2O_4$ and $FeCr_2O_4$) are detected due to metal oxidation at high temperature. The XRD pattern of Se/SSM is displayed in Fig. S1. Compared with that of the NiFeSe/SSM sample, the XRD pattern shows that Se and metal selenides are also produced on the surface of the SSM by the CVD process. Additionally, there are more noticeable metal oxides observed on the Se/SSM, which is attributed to those parts of the SSM that are not covered with Se by the CVD process. High-resolution X-ray photoelectron spectroscopy (HR-XPS) was performed to acquire the chemical states and bonding of Se, and the results are shown in Fig. 1(b). The distinct peaks at 55.56 eV and 56.42 eV, with an energy difference of 0.86 eV, in Se/SSM correspond to Se $3d_{5/2}$ and Se $3d_{3/2}$, respectively, which indicates that Se remains on the SSM surface after selenization and confirms the XRD observation. The deconvoluted peaks at 58.92 eV and 62.84 eV

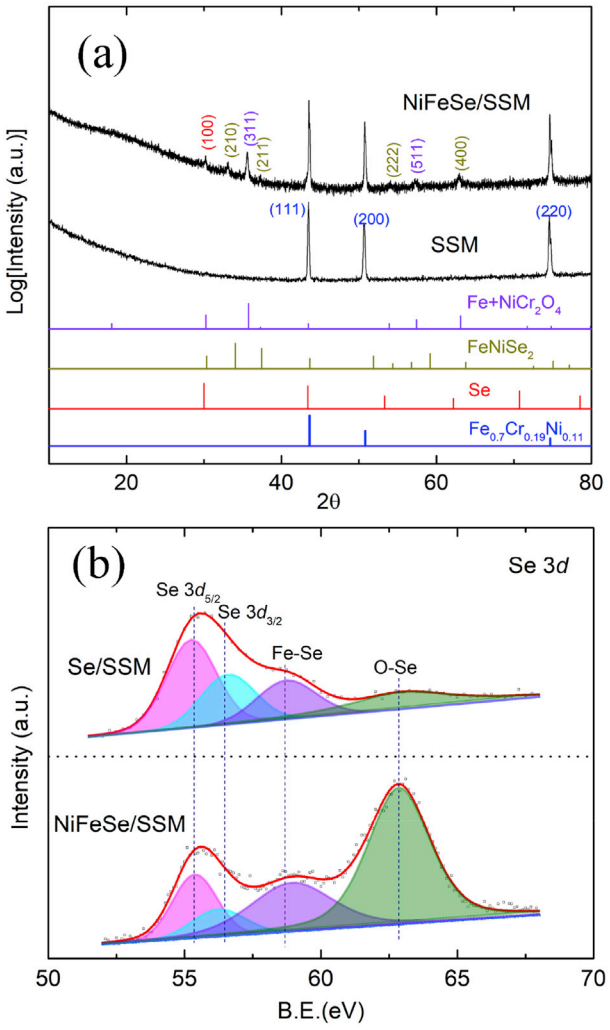

Fig. 1. (a) XRD patterns of as-received SSM and annealed NiFeSe/SSM with standard $Fe_{0.7}Cr_{0.19}Ni_{0.11}$ (PDF#33–0397), Se (PDF#38–0768), $NiFeSe_2$ (PDF#48–1881), and Fe + $NiCr_2O_4$ (PDF#23–1271). (b) Comparison of HR-XPS of Se 3*d* in Se/SSM and annealed NiFeSe/SSM. NiFeSe, nickel iron selenide; SSM, stainless steel mat; HR-XPS, high-resolution X-ray photoelectron spectroscopy

were assigned to the bonding of Fe–Se in $NiFeSe_2$ and to Se–O in oxides, respectively. The XPS spectrum of Se in NiFeSe/SSM exhibits a binding energy consistent with that for Se/SSM, suggesting that the same SSM surface chemical states remain after annealing. It can be proposed that Se undergoes the same chemical reaction and plays the same role in both Se/SSM and NiFeSe/SSM.

The surface morphologies of the as-received SSM and the surface-decorated SSM were investigated by scanning electron microscopy (SEM) and high-resolution transmission electron microscopy (HRTEM). Fig. 2(a) shows the smooth and clear surface of as-received SS under SEM. Its composition was further confirmed by X-ray energy dispersive spectrometry (Fig. S2), the results of which are comparable to those of the XRD analysis [Fig. 1(a)]. The surface of Se/SSM becomes noticeably rough after direct selenization by CVD, with microscale particles distributed lightly and unevenly on the SSM surface [Fig. 2(b)]. The randomly shaped and layered sheet can be clearly observed, which suggests successful selenization on the SSM surface [Fig. 2(b) and inset]. When the SSM loaded with the NiFeSe powder is annealed in the furnace, most of the SS surface area is homogeneously and densely covered by nanoscale and microscale particles [Fig. 2(c)]. In a high-

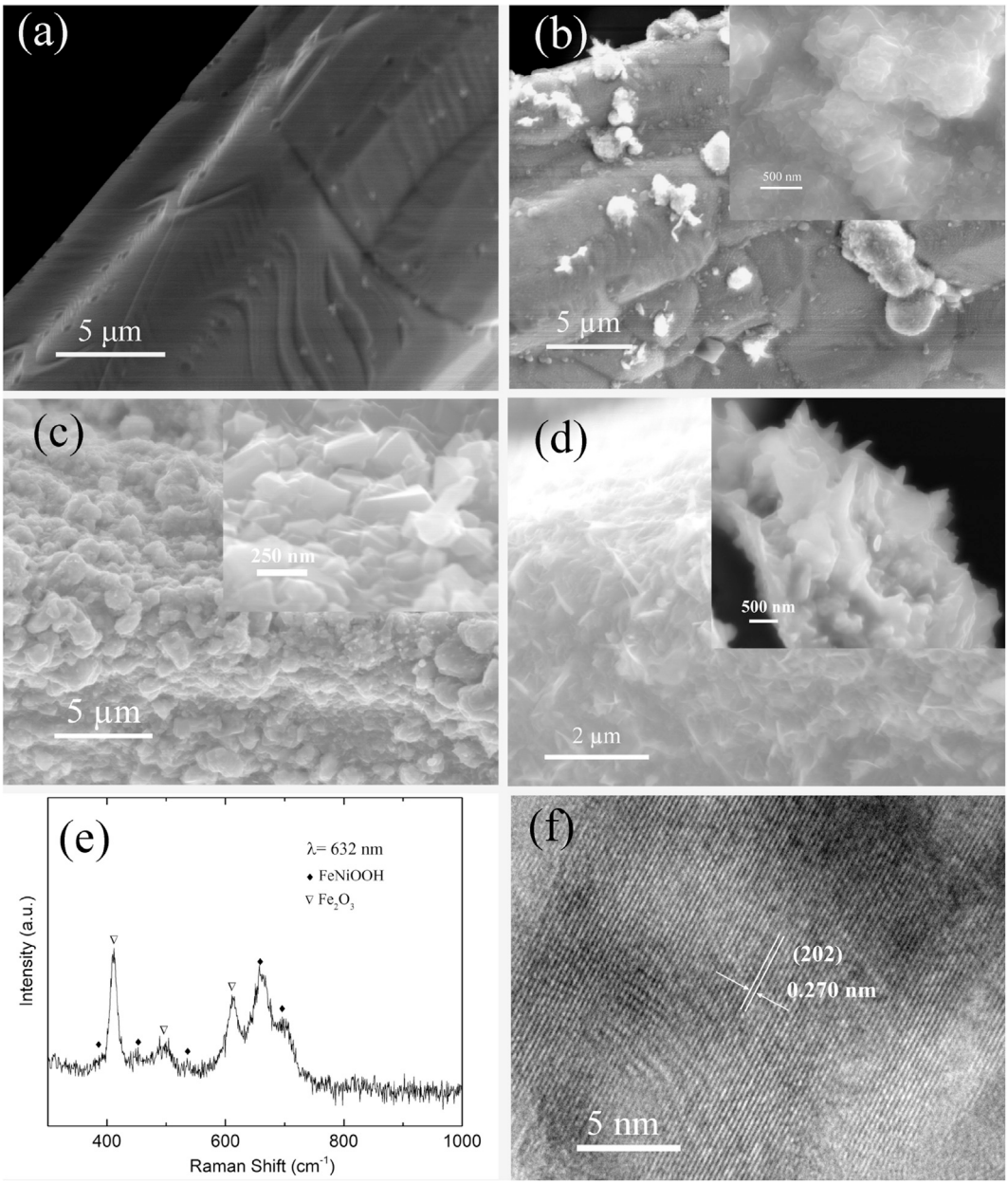

Fig. 2. SEM and HRTEM images of as-received SSM and surface-modified SSM. (a) SEM image of as-received SSM. (b) SEM image of Se/SSM after selenization by CVD. Inset: corresponding high-magnification image. (c) SEM image of annealed NiFeSe/SSM. Inset: corresponding high-magnification image. (d) SEM image of the NiFeSe/SSM surface after water oxidation. Inset: corresponding high-magnification image. (e) Raman spectra of annealed NiFeSe/SSM after OER. (f) HRTEM image of NiFeSe/SSM after water oxidation. NiFeSe, nickel iron selenide; SSM, stainless steel mat; SEM, scanning electron microscopy; HRTEM, high-resolution transmission electron microscopy; CVD, chemical vapor deposition.

magnification view [inset, Fig. 2(c)], these particles comprise well-crystallized nanoscale plates. Meanwhile, it is noticeable that direct selenization only results in the chemical reaction on the top fibers of the SSM, whereas immersion into the NiFeSe solution and the subsequent annealing result in reactions on all of the individual fibers of the SSM (Fig. S3). It was found here that the CVD procedure directly leads to the formation of metal selenides on the SSM surface. This apparently also explains why more metal oxides are observed on the Se/SSM following the CVD process, in comparison to NiFeSe/SSM. Similarly, selenization was found to be able to induce chemical bonding between the NiFeSe powder and the SSM rather than physical attachment. After tens of hours of OER performance tests, dense nanosheets are uniformly distributed on the surface of the NiFeSe/SSM sample [Fig. 2(d)]. It can be observed in the inset of Fig. 2(d) that these nanosheets along the fiber edges of the SSM are extremely thin, suggesting surface morphology reformation after OER. The subsequent Raman shift, shown in Fig. 2(e), verifies the main phase to be the FeNi (oxy)hydroxides on the surface, which is consistent with other reports [39,40]. The morphology of the thin nanosheets formed on the surface is also very similar with that reported for FeNiOOH [41]. The catalytically active metal (oxy)hydroxides were created by simple water oxidation from metal selenides in an alkaline solution, which has also been observed in other analogous experiments [27,42,43]. Fig. 2(f) shows the HRTEM image of the nanosheets produced on the NiFeSe/SSM surface. The lattice distance of 0.270 nm

corresponds to the (202) plane of the Fe oxyhydroxide, suggesting that the annealed NiFeSe particles are successfully converted to FeNiOOH by electrochemical oxidation. This conversion process can be well understood by repetitive CV in 1 M KOH during the initial activation process (Fig. S4). The anodic and cathodic peaks [denoted as A and C, respectively in Fig. S4(a)] are related to the absorption of OH and O radicals on the surface, in addition to the redox reaction of Ni^{2+}/Ni^{3+}, and the increase of charge capacity with increasing numbers of cycles [Fig. S4(b)] indicates the growth of hydroxides and the increased ECSA [22].

To further verify the reaction process, the chemical states of Fe in different samples were also investigated by HR-XPS, and the results are shown in Fig. 3(a). Two characteristic peaks of bare SSM at 708.04 eV and 721.69 eV, with an energy difference of 13.65 eV, are attributed to Fe $2p_{3/2}$ and Fe $2p_{1/2}$, respectively. They are accompanied by one satellite peak at 710.47 eV. In comparison, all of the peaks related to Fe are shifted to a higher binding energy after selenization or water oxidation. For example, the peaks of Fe 3*p* at 711.20 eV and 724.60 eV in Se/SSM, with an energy difference of 13.40 eV, are identified as Fe^{3+} $2p_{3/2}$ and Fe^{3+} $2p_{1/2}$, respectively. Two satellite peaks are located at 713.40 eV and 718.90 eV. It should be emphasized that the chemical states of Fe in Se/SSM and NiFeSe/SSM are almost identical. The Se bonding is also the same in both samples [Fig. 1(b)]. Se leads to the chemical bonding between the NiFeSe powder and the SSM through selenization. After water oxidation, Raman shift analyses [Fig. 2(e)] indicate the presence of FeNi (oxy)hydroxides on the SSM surface, which was also confirmed by XPS. The XPS deconvolution analyses of Cr 2*p* and Ni 2*p* are shown in Fig. S5. As seen in Fig. S5(a), no Cr 2*p* can be detected on the surface of the sample after water oxidation, which agrees with the final surface composition following the corrosion process and confirms that FeNiOOH is the active phase for OER [27,35]. Moreover, the amount of Cr is possibly outside the detection limit since NiFeSe powders decorate the surface. As shown in Fig. S5(b), Ni 2*p* exhibits a distinct shift to higher binding energy after water oxidation compared with the Ni 2*p* in SSM, and the peak centered at 856.10 eV is assigned to Ni $2p_{3/2}$ of FeNiOOH. Based on our aforementioned characterization and analysis, the role of Se over the whole synthesis process schematically illustrated in Fig. 3(b) might be described as follows:

$$Se + M \rightarrow MSe\ (M = Fe,\ Ni,\ Cr),$$

$$Se + M_2O_3 \rightarrow MSeO_2,$$

$$MSe + 8OH^- \rightarrow M(OH)_2 + SeO_3^{2-} + 3H_2O + 6e^-,$$

$$MSeO_2 + 4OH^- \rightarrow M(OH)_2 + SeO_4^{2-} + 3H_2O + 2e^-$$

The electrocatalytic OER performance parameters of SSM and NiFeSe/SSM are shown in Fig. 4. As shown in Fig. 4(a), the bare SSM shows a very high onset potential needed to cleave water and reaches a current density of 10 mA cm^{-2} at an overpotential of 340 mV, which is close to the reported performance of SS [27]. The control sample None/SSM can achieve a current density of 122 mA cm^{-2} at the same overpotential. The improvement is ascribed to the formation of metal oxides on the surface during annealing. When the SSM surface is engineered by Se, the catalytic performance is substantially increased. Se/SSM achieves current densities of 10 mA cm^{-2} and 100 mA cm^{-2} at overpotentials of 270 mV and 313 mV, respectively, which suggests that Se promotes the OER activity. After direct binding with NiFeSe powder, NiFeSe/SSM requires significantly lower overpotentials of 230 mV and 330 mV to achieve current densities of 10 mA cm^{-2} and 1,000 mA cm^{-2}, respectively. The further improvement of performance by NiFeSe/SSM in comparison with Se/SSM mainly results from the optimized NiFeSe powder. It can be observed that SSM with NiFeSe exhibits a distinct oxidation peak around 1.42–1.45 V

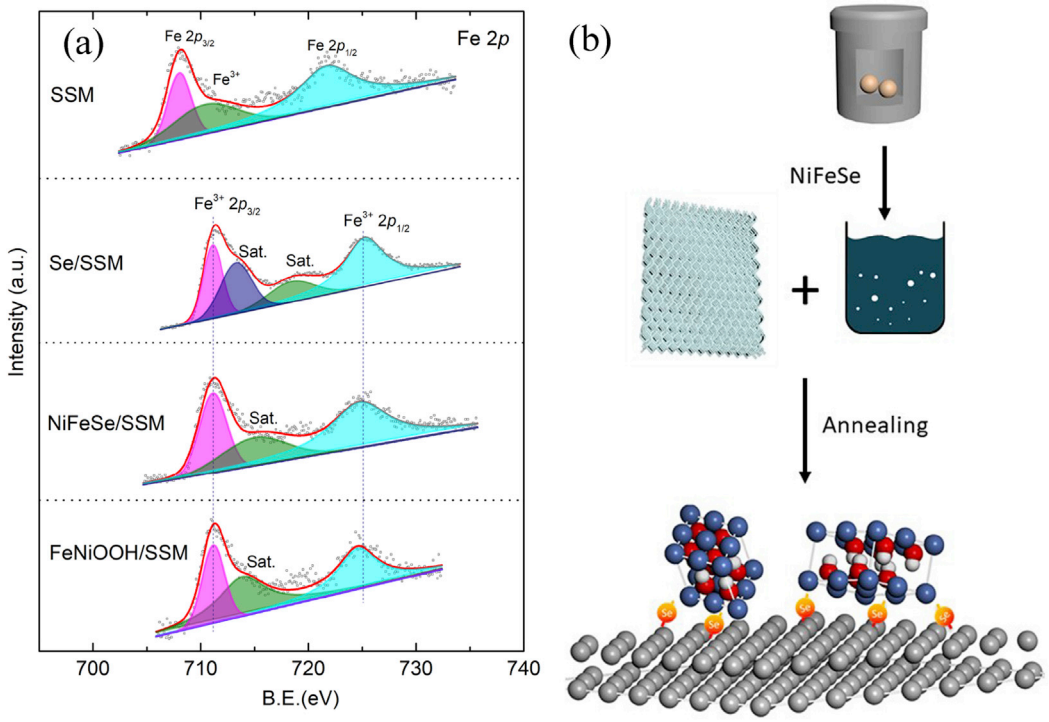

Fig. 3. (a) XPS of Fe 2*p* in as-received SSM and different surface-modified SSMs. (b) Schematic illustration of the NiFeSe/SSM synthesis process. NiFeSe, nickel iron selenide; SSM, stainless steel mat; XPS, X-ray photoelectron spectroscopy.

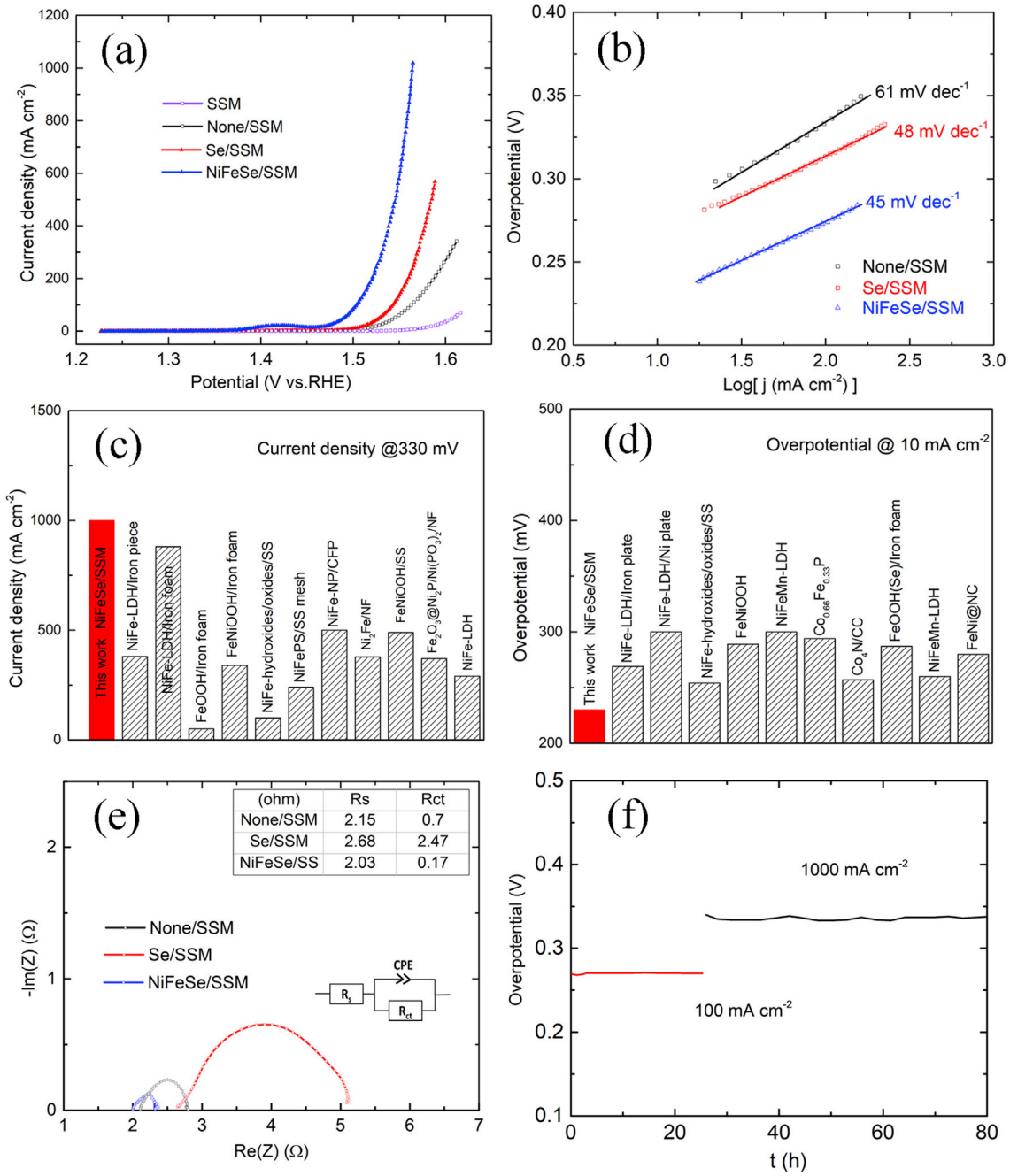

Fig. 4. Electrochemical characterization of SSM and surface-modified SSM for OER in 1 M KOH solution. (a) LSV curves and (b) corresponding Tafel slopes. Comparison of (c) driven current density at overpotential of 330 mV and (d) overpotential to provide current density of 10 mA cm^{-2} by SS-based and transition-metal-based catalysts (all data are corrected by iR compensation). (e) EIS with fitted Nyquist plots by a modified Randles circuit. (f) Stability evaluation based on chronopotentiometric curves over 80 h. NiFeSe, nickel iron selenide; SSM, stainless steel mat; EIS, electrochemical impedance spectroscopy; OER, oxygen evolution reaction; SS, stainless steel; LSV, linear sweep voltammetry.

(vs. RHE), and the corresponding reduction peak is also detected by CV scanning (Fig. S6). This peak is attributed to the chemical state variation of Ni between Ni^{2+} and Ni^{3+}. The emergence of the redox peak is mainly ascribed to the loaded NiFeSe powder because slightly increased Ni content is observed in annealed NiFeSe/SSM compared to the as-received SSM (Fig. S2). In order to differentiate their kinetics, the Tafel slopes of the samples were extracted directly from LSV and are shown in Fig. 4(b). Se/SSM exhibits a Tafel slope of 48 mV dec^{-1}, clearly lower than that of None/SSM (61 mV dec^{-1}), indicating the positive effect of Se in promoting OER [44,45]. The lowest Tafel slope of 45 mV dec^{-1} was obtained for NiFeSe/SSM, suggesting the highly catalytic kinetics of optimized NiFeSe. Compared with the most efficient OER catalysts based on SS, iron plate, iron foam, or other transition-metal nitrides or phosphides reported thus far, NiFeSe/SSM displays remarkable performance in driving current at 330 mV [Fig. 4(c) and Table S1] and its low overpotential needed to initiate current density of 10 mA cm^{-2} [Fig. 4(d) and Table S1].

To further clarify the reason underlying the high activity of NiFeSe/SSM for OER, the ECSA and the electrochemical impedance spectroscopy (EIS) of the samples were explored. ECSA was acquired according to the capacitance, which was extracted by the

capacitive current density against the scan rate in the non-Faradic zone. As shown in Fig. S7, Se/SSM and None/SSM exhibit similar ECSA values, 3.8 mF cm^{-2} and 3.7 mF cm^{-2}, respectively. The ECSA of NiFeSe/SSM is 5.5 mF cm^{-2}, 45% higher than that of None/SSM. The higher active surface area of NiFeSe/SSM is attributed to its rough surface after NiFeSe powder decoration. The large ECSA also contributes to the highly efficient OER activity of NiFeSe/SSM. As shown by the EIS analysis in Fig. 4(e), all of the electrodes exhibit comparable internal charge-transfer resistance values. However, NiFeSe/SSM exhibits extremely low charge-transfer resistance of 0.17 Ω at the electrode/electrolyte interface, which is far lower than that of None/SSM and Se/SSM, and almost 50% lower than that obtained by corrosion engineering [34]. The low charge transfer barrier at the electrode/electrolyte interface demonstrates that the combination of NiFeSe and SSM is advantageous for achieving highly efficient OER.

Robust durability and stability are prerequisites for good catalysts. Chronopotentiometric measurements were conducted to evaluate the stability of the NiFeSe/SSM catalyst, and the results are displayed in Fig. 4(f). The catalyst is able to first sustain a current density of 100 mA cm^{-2} for 25 h and subsequently to endure a current density of 1,000 mA cm^{-2} for 55 h, finally presenting negligible voltage drift and demonstrating extraordinary structure and catalytic stability for OER (Fig. S8).

To verify our proposed synthesis route, we combined the optimized NiFeSe powder with NF. The electrochemical catalytic activity of NiFeSe/NF is shown in Fig. S9. NiFeSe/NF achieves a current density of 1,000 mA cm^{-2} at an overpotential of 288 mV. Physically, NF has the advantage of higher porosity in comparison with SSM, which leads to the better OER performance of NiFeSe/NF. Thus, enhancing porosity might be a feasible way to further improve the catalytic activity of SSM-based catalysts.

Industrial water electrolysis is carried out at 60°C–70°C to further reduce the overpotential. Therefore, the OER performance of NiFeSe/SSM was investigated in 1 M KOH at different temperatures (Fig. S10). At 75°C, NiFeSe/SSM displays remarkable performance, achieving a current density of 1,000 mA cm^{-2} at an overpotential of 260 mV, 70 mV lower than that needed to achieve the same current density at 22°C [Fig. 4(a)]. The superior OER performance and robust durability of, and the cost-effective synthesis process for, the NiFeSe/SSM catalyst suggest its promising future for water splitting.

Conclusions

The surface of a SSM was successfully engineered by binding optimized NiFeSe to it through selenization. It was suggested that Se is effective in inducing an active catalytic phase and promoting the OER kinetics. Benefiting from the strong covalent bonding between the SSM and the NiFeSe, NiFeSe/SSM displays low charge-transfer resistance and robust durability against the strong gas bubbles, which contribute to a current density of 1,000 mA cm^{-2} at an overpotential of 330 mV in 1 M KOH at room temperature. The overpotential shows negligible degradation after 55 h of testing under this current density. At 75°C, NiFeSe/SSM can achieve a current density of 1,000 mA cm^{-2} at an overpotential of 260 mV. This work thus provides an innovative route to turn SS into an excellent electrocatalyst and substrate for efficient oxygen evolution reaction.

Author contributions

S. Song and Z. Ren conceptualized and validated this work. Z. Ren and H. Zhou contributed to the funding acquisition. All authors took part in the investigation and data analysis. Everyone was involved in writing the paper.

Declaration of competing interest

The authors declare no competing financial interest.

Acknowledgments

Z.R. acknowledges the Research Award from the Alexander von Humboldt Foundation and Professor Kornelius Nielsch at IFW Dresden in Germany.

Appendix A. Supplementary data

Supplementary data to this article can be found online at https://doi.org/10.1016/j.mtphys.2020.100216.

References

[1] J. Kibsgaard, I. Chorkendorff, Considerations for the scaling-up of water splitting catalysts, Nat. Energy 4 (2019) 430.
[2] F. Yu, L. Yu, I.K. Mishra, Y. Yu, Z.F. Ren, H.Q. Zhou, Recent developments in earth-abundant and non-noble electrocatalysts for water electrolysis, Mater, Today Phys. 7 (2018) 121.
[3] X. Tian, P. Zhao, W. Sheng, Hydrogen evolution and oxidation: mechanistic studies and material advances, Adv. Mater. 31 (2019) 1808066.
[4] S.W. Song, J. Mao, M. Bordelon, R. He, Y.M. Wang, J. Shuai, J.Y. Sun, X.B. Lei, Z.S. Ren, S. Chen, S. Wilson, K. Nielsch, Q.Y. Zhang, Z.F. Ren, Joint effect of magnesium and yttrium on enhancing thermoelectric properties of n-type Zintl $Mg_{3+\delta}Y_{0.02}Sb_{1.5}Bi_{0.5}$, Mater, Today Phys. 8 (2019) 25–33.
[5] Y. Li, X. Du, J. Huang, C. Wu, Y. Sun, G. Zou, C. Yang, J. Xiong, Recent progress on surface reconstruction of earth-abundant electrocatalysts for water oxidation, Small 15 (2019) 1901980.
[6] B. You, Y. Sun, Innovative strategies for electrocatalytic water splitting, Acc. Chem. Res. 51 (2018) 1571–1580.
[7] L. Jiang, S. Song, D. Luo, F. Cai, L. Xie, Q. Zhang, Z. Ren, Plant growth–inspired design of high-performance composite electrode nanostructures for supercapacitors, Mater. Today Phys. (2019) 100138.
[8] C. Lei, S. Lyu, J. Si, B. Yang, Z. Li, L. Lei, Z. Wen, G. Wu, Y. Hou, Nanostructured carbon based heterogeneous electrocatalysts for oxygen evolution reaction in alkaline media, ChemCatChem 11 (2019) 5855.
[9] H. Zhou, F. Yu, Q. Zhu, J. Sun, F. Qin, L. Yu, J. Bao, Y. Yu, S. Chen, Z. Ren, Water splitting by electrolysis at high current densities under 1.6 volts, Energy Environ. Sci. 11 (2018) 2858.
[10] F. Yu, H. Zhou, Y. Huang, J. Sun, F. Qin, J. Bao, W.A. Goddard, S. Chen, Z. Ren, High-performance bifunctional porous non-noble metal phosphide catalyst for overall water splitting, Nat. Commun. 9 (2018) 2551.
[11] P. Zhang, L. Li, D. Nordlund, H. Chen, L. Fan, B. Zhang, X. Sheng, Q. Daniel, L. Sun, Dendritic core-shell nickel-iron-copper metal/metal oxide electrode for efficient electrocatalytic water oxidation, Nat. Commun. 9 (2018) 381.
[12] J. Guan, Z. Duan, F. Zhang, S.D. Kelly, R. Si, M. Dupuis, Q. Huang, J.Q. Chen, C. Tang, C. Li, Water oxidation on a mononuclear manganese heterogeneous catalyst, Nat. Catal. 1 (2018) 870–877.
[13] Y. Zhu, G. Chen, Y. Zhong, Y. Chen, N. Ma, W. Zhou, Z. Shao, A surface-modified antiperovskite as an electrocatalyst for water oxidation, Nat. Commun. 9 (2018) 2326.
[14] X. Cheng, Z. Pan, C. Lei, Y. Jin, B. Yang, Z. Li, X. Zhang, L. Lei, C. Yuan, Y. Hou, A strongly coupled 3D ternary Fe_2O_3@Ni_2P/$Ni(PO_3)_2$ hybrid for enhanced electrocatalytic oxygen evolution at ultra-high current densities, J. Mater. Chem. 7 (2019) 965–971.
[15] B.H.R. Suryanto, Y. Wang, R.K. Hocking, W. Adamson, C. Zhao, Overall electrochemical splitting of water at the heterogeneous interface of nickel and iron oxide, Nat. Commun. 10 (2019) 5599.
[16] M.E.G. Lyons, M.P. Brandon, A comparative study of the oxygen evolution reaction on oxidised nickel, cobalt and iron electrodes in base, J. Electroanal. Chem. 641 (2010) 119–130.
[17] J. Sun, M. Ren, L. Yu, Z. Yang, L. Xie, F. Tian, Y. Yu, Z. Ren, S. Chen, H. Zhou, Highly efficient hydrogen evolution from a mesoporous hybrid of nickel phosphide nanoparticles anchored on cobalt phosphosulfide/phosphide nanosheet arrays, Small 15 (2019) 1804272.
[18] H. Zhang, H.T. Chung, D.A. Cullen, S. Wagner, U.I. Kramm, K.L. More, P. Zelenay, G. Wu, High-performance fuel cell cathodes exclusively containing atomically dispersed iron active sites, Energy Environ. Sci. 12 (2019) 2548.
[19] J. Zhu, Z.C. Wang, H. Dai, Q. Wang, R. Yang, H. Yu, M. Liao, J. Zhang, W. Chen, Z. Wei, N. Li, L. Du, D. Shi, W. Wang, L. Zhang, Y. Jiang, G. Zhang, Boundary activated hydrogen evolution reaction on monolayer MoS_2, Nat. Commun. 10 (2019) 1348.

[20] D. Vikraman, S. Hussain, K. Akbar, K. Adaikalam, S.H. Lee, S.-H. Chun, J. Jung, H.-S. Kim, H.J. Park, Facile synthesis of molybdenum diselenide layers for high-performance hydrogen evolution electrocatalysts, ACS Omega 3 (2018) 5799.
[21] S. Song, L. Yu, V. Hadjiev, W. Zhang, D. Wang, X. Xiao, S. Chen, Q. Zhang, Z. Ren, A new way to synthesize robust and porous $Ni_{1-x}Fe_x$ layered double hydroxide for efficient electrocatalytic oxygen evolution, ACS Appl. Mater. Interfaces 11 (2019) 32909.
[22] M.E. Lyons, R. Doyle, Enhanced oxygen evolution at hydrous oxy-hydroxide modified iron electrodes in aqueous alkaline solution, Int. J. Electrochem. Sci. 6 (2011) 5710.
[23] K.C. Leonard, M.I. Tejedor-Anderson, M.A. Anderson, Nanoporous oxide coatings on stainless steel to enable water splitting and reduce the hydrogen evolution overpotential, Int. J. Hydrogen Energy 37 (2012) 18654.
[24] H. Schäfer, S.M. Beladi-Mousavi, L. Walder, J. Wollschläger, O. Kuschel, S. Ichilmann, S. Sadaf, M. Steinhart, K. Küpper, L. Schneider, Surface oxidation of stainless steel: oxygen evolution electrocatalysts with high catalytic activity, ACS Catal. 5 (2015) 2671.
[25] H. Schäfer, M. Chatenet, Steel: the resurrection of a forgotten water-splitting catalyst, ACS Energy Lett. 3 (2018) 574–591.
[26] F. Yu, F. Li, L. Sun, Stainless steel as an efficient electrocatalyst for water oxidation in alkaline solution, Int. J. Hydrog. Energy 41 (2016) 5230.
[27] D. Tang, O. Mabayoje, Y. Lai, Y. Liu, C.B. Mullins, In situ growth of Fe(Ni)OOH catalyst on stainless steel for water oxidation, Chem. Select. 2 (2017) 2230.
[28] S. Anantharaj, M. Venkatesh, A.S. Salunke, T.V.S.V. Simha, V. Prabu, S. Kundu, High-performance oxygen evolution anode from stainless steel via controlled surface oxidation and Cr removal, ACS Sustain. Chem. Eng. 5 (2017) 10072.
[29] M. Yao, H. Hu, N. Wang, W. Hu, S. Komarneni, Quaternary (Fe/Ni)(P/S) mesoporous nanorods templated on stainless steel mesh lead to stable oxygen evolution reaction for over two months, J. Colloid Interface Sci. 561 (2019) 576.
[30] N. Todoroki, T. Wadayama, Heterolayered Ni–Fe hydroxide/oxide nanostructures generated on a stainless-steel substrate for efficient alkaline water splitting, ACS Appl. Mater. Interfaces 11 (2019) 44161.
[31] J. Jiang, F. Sun, S. Zhou, W. Hu, H. Zhang, J. Dong, Z. Jiang, J. Zhao, J. Li, W. Yan, M. Wang, Atomic-level insight into super-efficient electrocatalytic oxygen evolution on iron and vanadium co-doped nickel (oxy)hydroxide, Nat. Commun. 9 (2018) 2885.
[32] S. Fu, J. Song, C. Zhu, G.-L. Xu, K. Amine, C. Sun, X. Li, M.H. Engelhard, D. Du, Y. Lin, Ultrafine and highly disordered Ni_2Fe_1 nanofoams enabled highly efficient oxygen evolution reaction in alkaline electrolyte, Nano Energy 44 (2018) 319.
[33] I. Barauskienė, E. Valatka, Layered nickel-cobalt oxide coatings on stainless steel as an electrocatalyst for oxygen evolution reaction, Electrocatalysis 10 (2018) 63.
[34] Y. Liu, X. Liang, L. Gu, Y. Zhang, G.D. Li, X. Zou, J.S. Chen, Corrosion engineering towards efficient oxygen evolution electrodes with stable catalytic activity for over 6000 hours, Nat. Commun. 9 (2018) 2609.
[35] H. Schäfer, S. Sadaf, L. Walder, K. Kuepper, S. Dinklage, J. Wollschläger, L. Schneider, M. Steinhart, J. Hardege, D. Daum, Stainless steel made to rust: a robust water-splitting catalyst with benchmark characteristics, Energy Environ. Sci. 8 (2015) 2685.
[36] W. Li, D. Xiong, X. Gao, L. Liu, The oxygen evolution reaction enabled by transition metal phosphide and chalcogenide pre-catalysts with dynamic changes, Chem. Commun. 55 (2019) 8744.
[37] X. Long, J. Li, S. Xiao, K. Yan, Z. Wang, H. Chen, S. Yang, A strongly coupled graphene and FeNi double hydroxide hybrid as an excellent electrocatalyst for the oxygen evolution reaction, Angew Chem. Int. Ed. Engl. 53 (2014) 7584.
[38] M.W. Louie, A.T. Bell, An investigation of thin-film Ni-Fe oxide catalysts for the electrochemical evolution of oxygen, J. Am. Chem. Soc. 135 (2013) 12329.
[39] M. Legodi, D. Dewaal, The preparation of magnetite, goethite, hematite and maghemite of pigment quality from mill scale iron waste, Dyes Pigments 74 (2007) 161.
[40] D.T.M. Phan, T. Häger, W. Hofmeister, The influence of the Fe_2O_3 content on the Raman spectra of sapphires, J. Raman Spectrosc. 48 (2017) 453.
[41] H. Zhong, J. Wang, F. Meng, X. Zhang, In situ activating ubiquitous rust towards low-cost, efficient, free-standing, and recoverable oxygen evolution electrodes, Angew Chem. Int. Ed. Engl. 55 (2016) 9937.
[42] X. Xu, F. Song, X. Hu, A nickel iron diselenide-derived efficient oxygen-evolution catalyst, Nat. Commun. 7 (2016) 12324.
[43] O. Diaz-Morales, I. Ledezma-Yanez, M.T.M. Koper, F. Calle-Vallejo, Guidelines for the rational design of Ni-based double hydroxide electrocatalysts for the oxygen evolution reaction, ACS Catal. 5 (2015) 5380.
[44] H. Cheng, Z. Cao, Z. Chen, M. Zhao, M. Xie, Z. Lyu, Z. Zhu, M. Chi, Y. Xia, Catalytic system based on sub-2 nm Pt particles and its extraordinary selectivity and durability for oxygen reduction, Nano Lett. 19 (2019) 4997.
[45] S. Niu, W.-J. Jiang, Z. Wei, T. Tang, J. Ma, J.-S. Hu, L.-J. Wan, Se-doping activates FeOOH for cost-effective and efficient electrochemical water oxidation, J. Am. Chem. Soc. 141 (2019) 7005.